Ann. Appl. Math.
doi: 10.4208/aam.OA-2024-0003

Vol. **40**, No. 2, pp. 1-22
xxx 2024

On a Hybrid Method for Inverse Transmission Eigenvalue Problems

Weishi Yin[1], Zhaobin Xu[1], Pinchao Meng[1] and Hongyu Liu[2,*]

[1] *School of Mathematics and Statistics, Changchun University of Science and Technology, Changchun, Jilin 130022, China*

[2] *Department of Mathematics, City University of Hong Kong, Kowloon, Hong Kong, China*

Received 19 January 2024; Accepted (in revised version) 14 March 2024

Abstract. In this paper, we are concerned with the inverse transmission eigenvalue problem to recover the shape as well as the constant refractive index of a penetrable medium scatterer. The linear sampling method is employed to determine the transmission eigenvalues within a certain wavenumber interval based on far-field measurements. Based on a prior information given by the linear sampling method, the neural network approach is proposed for the reconstruction of the unknown scatterer. We divide the wavenumber intervals into several subintervals, ensuring that each transmission eigenvalue is located in its corresponding subinterval. In each such subinterval, the wavenumber that yields the maximum value of the indicator functional will be included in the input set during the generation of the training data. This technique for data generation effectively ensures the consistent dimensions of model input. The refractive index and shape are taken as the output of the network. Due to the fact that transmission eigenvalues considered in our method are relatively small, certain super-resolution effects can also be generated. Numerical experiments are presented to verify the effectiveness and promising features of the proposed method in two and three dimensions.

AMS subject classifications: 35P25, 35R30, 35P15

Key words: Inverse transmission eigenvalue problem, linear sampling method, neural network, super-resolution.

*Corresponding author.
Emails: yinweishi@cust.edu.cn (W. Yin), xuzhaobin@mails.cust.edu.cn (Z. Xu), mengpc@cust.edu.cn (P. Meng), hongyliu@cityu.edu.hk (H. Liu)

1 Introduction

In this paper, we are mainly concerned with the interior transmission eigenvalue problem and its applications to the inverse scattering problem. This problem has received considerable interest in the literature in recent years [10, 14]. In what follows, we first present the mathematical formulation of our study.

Let $D_0 \subset \mathbb{R}^n$ $(n=2,3)$ be a bounded and simply connected domain with a smooth boundary Γ_0. The incident field is given by the time-harmonic plane wave in the form

$$u^i(x) := e^{\mathrm{i}kx\cdot d}, \tag{1.1}$$

where $k \in \mathbb{R}_+$ is the wavenumber, $d \in \mathbb{S}^{n-1} := \{x \in \mathbb{R}^n; |x| = 1\}$ is the incident direction and $\mathrm{i} := \sqrt{-1}$. The exterior scattering problem is to find the total field $u = u^s(x,d,D_0) + u^i(x)$ and the transmitted field u_0 satisfying

$$\begin{cases} \Delta u + k^2 u = 0 & \text{in } \mathbb{R}^n \backslash \overline{D_0}, \\ \Delta u_0 + k^2 n_0 u_0 = 0 & \text{in } D_0, \\ u - u_0 = 0, \quad \dfrac{\partial u}{\partial \nu} - \dfrac{\partial u_0}{\partial \nu} = 0 & \text{on } \Gamma_0, \\ \lim\limits_{r\to\infty} r^{\frac{n-1}{2}} \left(\dfrac{\partial u^s(x,d,D_0)}{\partial r} - \mathrm{i}k u^s(x,d,D_0) \right) = 0, & r = |x|, \end{cases} \tag{1.2}$$

where $n_0 \in L^\infty(D_0)$ is the positive refractive index and ν is the unit outward normal. There exists a unique solution $u_0\chi_{D_0} + u\chi_{\mathbb{R}^n\backslash\overline{D}_0} \in H^1_{loc}(\mathbb{R}^n)$ to the problem (1.2) (cf. [21]). The associated interior transmission eigenvalue problem to (1.2) for non-trivial $(v,w) \in L^2(D_0) \times L^2(D_0)$ can be described by

$$\begin{cases} \Delta v + k^2 v = 0 & \text{in } D_0, \\ \Delta w + k^2 n_0 w = 0 & \text{in } D_0, \\ v - w = 0, \quad \dfrac{\partial v}{\partial \nu} - \dfrac{\partial w}{\partial \nu} = 0 & \text{on } \Gamma_0. \end{cases} \tag{1.3}$$

The wavenumber $k \in \mathbb{R}_+$ is called an interior transmission eigenvalues with the associated transmission eigenfunctions v, w. In order to generate certain super-resolution effects, a relatively large refractive index should be chosen to obtain the relatively small transmission eigenvalues. For practical considerations, we assume that the refractive index of the medium scatterer D_0 is relatively small. In order to produce the super-resolution effect, we introduce a thin coating D_1 on the domain D_0 (see Fig. 1), $\Gamma_1 := \partial D_1$. The refractive index n_1 in D_1 is far larger than n_0 in D_0, i.e., $n_0 \ll n_1$. For the subsequent discussion, we regard the domains D_1 and D_0 as the

two-layer medium. In this case, the exterior scattering problem becomes to find the total field $u=u^s(x,d,D_0,D_1)+u^i(x)$ and the transmitted field u_0, u_1 such that

$$\begin{cases} \Delta u+k^2u=0 & \text{in } \mathbb{R}^n\backslash\overline{D_0\cup D_1}, \\ \Delta u_1+k^2n_1u_1=0 & \text{in } D_1, \\ \Delta u_0+k^2n_0u_0=0 & \text{in } D_0, \\ u-u_1=0, \quad \dfrac{\partial u}{\partial\nu}-\dfrac{\partial u_1}{\partial\nu}=0 & \text{on } \Gamma_1, \\ u_1-u_0=0, \quad \dfrac{\partial u_1}{\partial\nu}-\dfrac{\partial u_0}{\partial\nu}=0 & \text{on } \Gamma_0, \\ \lim\limits_{r\to\infty} r^{\frac{n-1}{2}}\left(\dfrac{\partial u^s(x,d,D_0,D_1)}{\partial r}-\mathrm{i}ku^s(x,d,D_0,D_1)\right)=0, & r=|x|. \end{cases} \tag{1.4}$$

Similarly, the corresponding interior transmission eigenvalue problem can be written in the following form

$$\begin{cases} \Delta v+k^2v=0 & \text{in } D_0\cup D_1, \\ \Delta w_++k^2n_1w_+=0 & \text{in } D_1, \\ \Delta w_-+k^2n_0w_-=0 & \text{in } D_0, \\ v-w_+=0, \quad \dfrac{\partial v}{\partial\nu}-\dfrac{\partial w_+}{\partial\nu}=0 & \text{on } \Gamma_1, \\ w_+-w_-=0, \quad \dfrac{\partial w_+}{\partial\nu}-\dfrac{\partial w_-}{\partial\nu}=0 & \text{on } \Gamma_0. \end{cases} \tag{1.5}$$

For convenience, the scattered field $u^s(x,d,D_0)$ and $u^s(x,d,D_0,D_1)$ are both named as $u^s(x,d)$. This scattered field $u^s(x,d)$ has the following asymptotic expansion

$$u^s(x,d)=\gamma_n\frac{e^{ikr}}{r^{\frac{n-1}{2}}}\left\{u^\infty(\hat{x},d)+\mathcal{O}\left(\frac{1}{r}\right)\right\}, \quad r=|x|\to\infty, \tag{1.6}$$

which holds uniformly for all observation directions $\hat{x}=x/|x|$, where

$$\gamma_n=\begin{cases} \dfrac{\mathrm{e}^{\mathrm{i}\pi/4}}{\sqrt{8k\pi}}, & n=2, \\ \dfrac{1}{4\pi}, & n=3, \end{cases}$$

and $u^\infty(\hat{x},d)$ is regarded as the far-field pattern of $u^s(x,d)$.

The transmission eigenvalue problem has been extensively investigated in recent years [1, 4, 9, 10, 14, 18, 19, 22, 32, 35, 36]. And it is well known that the transmission eigenvalues $k\in\mathbb{R}_+$ can be determined from far-field measurements $u^\infty(\hat{x},d)$ using

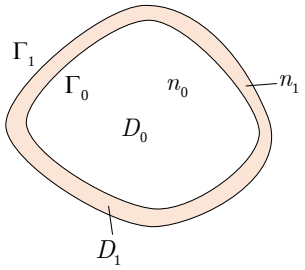

Figure 1: Sketch of the geometry.

sampling type method [8,10,19]. We also refer the readers to [1,5,12,29,33,34] and the references therein for other computational methods. Such eigenvalues encode the physical information of the scatterer. Therefore, one can further recover the physical properties of the scatterer with the transmission eigenvalues [7,10,13,23,24]. In particular, we would like to point out that in [10] surface-localized eigenstates are employed for the qualitative imaging of the shape of the medium scatterer with small eigenvalues, which can produce super-resolution imaging effects. The transmission eigenvalues are also related to invisibility cloaks [2,3,18,22,25].

In this paper, we propose a new scheme which consists of two phases for this kind of the inverse transmission eigenvalue problem. In the first phase, we employ the linear sampling method to determine the transmission eigenvalues within certain wavenumber intervals. The linear sampling method has been successfully developed for inverse scattering problems [10,11,31]. In the second phase, a neural network approach is used to obtain the reconstructions of the shape and material property. Recently, neural network has been applied for various inverse problems; see [15, 16,20,28] and the references therein. By a large number of training data, neural network can effectively learn the abstract relationship between model input and output, and reduce the impact of noise. Compared to the classical methods, neural network deals with the inverse problem from the perspective of data driven, which makes it possible for many more challenging problems [26,27,30]. In our neural network scheme, we first divide the wavenumber intervals into some subintervals based on prior information from the linear sampling method. Each transmission eigenvalue is located in the corresponding subinterval. For each subinterval, the wavenumber that corresponds to the maximum value of the indicator function will be included in the input set for training data. This data generation technique effectively ensures consistent dimensions of the input for the neural network. The constant refractive index and shape are regarded as the model output. Because the transmission eigenvalues considered in our method are relatively small, certain super-resolution effects can also be generated.

The rest of the paper is arranged as follows. In Section 2, the linear sampling method (LSM) is proposed to determine the transmission eigenvalues with far-field measurements. In Section 3, we employ the neural network method to reconstruct the shape and refractive index of the unknown scatterer. In Section 4, some numerical examples are presented to demonstrate the effectiveness of the proposed scheme. Finally, the paper is concluded in Section 5 with some relevant discussions.

2 Determination of the transmission eigenvalues

In this section, the LSM is employed to determine the transmission eigenvalues within the interval $I:=(\kappa_0,\kappa_1)$ using the knowledge of the far-field measurements $u^\infty(\hat{x},d)$. This methodology follows the spirit of [8, 10]. To that end, we define the far-field operator $F:L^2(\mathbb{S}^{n-1})\to L^2(\mathbb{S}^{n-1})$ as

$$(F\mathrm{g})(\hat{x}):=\int_{\mathbb{S}^{n-1}} u^\infty(\hat{x},d)\mathrm{g}(d)ds(d),\quad \hat{x}\in\mathbb{S}^{n-1}, \tag{2.1}$$

and the Herglotz wave function as

$$v_g(x):=\int_{\mathbb{S}^{n-1}} \mathrm{e}^{ikx\cdot d}\mathrm{g}(d)ds(d),\quad x\in\mathbb{R}^n. \tag{2.2}$$

The key to the LSM is to find a regularized solution $\mathrm{g}\in L^2(\mathbb{S}^{n-1})$ which satisfies the following first-kind integral equation

$$\gamma_n F\mathrm{g}=\Phi^\infty, \tag{2.3}$$

where

$$\Phi^\infty=\begin{cases}\dfrac{e^{i\pi/4}}{\sqrt{8\pi k}}e^{-ik\hat{x}\cdot z}, & n=2,\\ \dfrac{1}{4\pi}e^{-ik\hat{x}\cdot z}, & n=3,\end{cases}$$

is the far-field pattern of $\Phi(x,z)$. $\Phi(x,z)$ signifies the fundamental solution to the partial differential operator $-\Delta-k^2$, which is given as

$$\Phi(x,z)=\begin{cases}\dfrac{i}{4}H_0^{(1)}(k|x-z|), & n=2,\\ \dfrac{\mathrm{e}^{\mathrm{i}k|x-z|}}{4\pi|x-z|}, & n=3.\end{cases}$$

$H_0^{(1)}$ denotes the Hankel function of the first kind of order zero. We define $D=D_0$ for (1.2) and $D=D_0\cup D_1$ for (1.4). Then in what follows, we introduce the fundamental theorem of the linear sampling method (cf. [6]).

Theorem 2.1. *If k is not a transmission eigenvalue in D and $z\in D$, then for every $\delta>0$, there exists $\mathrm{g}_z^\delta\in L^2(\mathbb{S}^{n-1})$ such that*

$$\|F\mathrm{g}_z^\delta-\Phi^\infty\|_{L^2(\mathbb{S}^{n-1})}<\delta,$$

and $v_{\mathrm{g}_z^\delta}(x)$ converges in the $H^1(D)$ norm when $\delta\to 0$.

In this paper, we are more concerned with the case when k is a transmission eigenvalue. From the results in [8], we know that in this case Theorem 2.1 will not work. To that end, let F^δ be the far-field operator corresponding to the noisy measurement

$$(F^\delta \mathrm{g})(\hat{x}):=\int_{\mathbb{S}^{n-1}} u^{\infty,\delta}(\hat{x},d)\mathrm{g}(d)ds(d),\quad \hat{x}\in\mathbb{S}^{n-1}, \tag{2.4}$$

where δ is the noise level. The behavior of $v_{\mathrm{g}_z^\delta}(x)$ is described in the following theorem when k is a transmission eigenvalue.

Theorem 2.2. *If k is a transmission eigenvalue in D and for all points $z\in D$ the assumption*

$$\lim_{\delta\to 0}\|F^\delta \mathrm{g}_z^\delta-\Phi^\infty\|_{L^2(\mathbb{S}^{n-1})}=0$$

holds, then for every $\delta>0$, there exists $\|v_{\mathrm{g}_z^\delta}\|_{H^1(D)}$ can not be bounded when $\delta\to 0$.

The proofs for $D=D_0$ and $D=D_0\cup D_1$ are similar in the above two theorems and thus we omit them here. From these two theorems, we find that the value of $\|\mathrm{g}_z^\delta\|_{L^2(\mathbb{S}^{n-1})}$ will be relatively large for k is a transmission eigenvalue and relatively small otherwise. Hence, $\|\mathrm{g}_z^\delta\|_{L^2(\mathbb{S}^{n-1})}$ can be used to determine the transmission eigenvalues. We refer the readers to Algorithm 3.1 in [10] for the details of this idea.

3 Reconstruction of the scatterer

In this section, a deep residual neural network method is presented to recover the physical properties of the scatterer by the corresponding transmission eigenvalues. The refractive index we consider in this section is real constant, and for the case of complex constant our method can also work well. According to the discussions in the above section, one can determine the transmission eigenvalues within the interval $I:=(\kappa_0,\kappa_1)$. Let $K=\{k_i,\ i=1,2,\cdots,N_k\}$ be the true eigenvalues in I determined using the far-field measurements obtained by the linear sampling method. The wavenumber interval I can be divided into $I=\bigcup_{i=1}^{N_k} I_i$, and each k_i is in the corresponding subinterval I_i. Hence, the definition of model input is introduced as follows.

Definition 3.1. *Let I_i denote the ith subinterval of I with $I=\bigcup_{i=1}^{N_k} I_i$. The input of the neural network is given by*

$$X=(X_1,X_2,\cdots,X_{N_k})\in\mathbb{R}^{N_k}, \tag{3.1}$$

where $X_i\in I_i$ is the corresponding wavenumber which can get the maximum of $\|\mathrm{g}_z^{\varepsilon}\|_{L^2(\mathrm{S}^{n-1})}$ in I_i.

We would like to emphasize that X_i is different from k_i. k_i is the true eigenvalue while X_i is the input data of our network generated in the interval I_i. The purpose that we make use of this kind of data is to ensure the same dimensions of the model input. To define the form of the model output, we first set a reasonable parameterization of the scatterer.

Assumption 3.1. In 2D, we suppose the scatterer D_0 is a starlike domain with respect to the origin whose boundary Γ_0 can be represented as

$$\Gamma_0=r_0(\theta)(\cos\theta,\sin\theta),\quad 0\le\theta\le 2\pi, \tag{3.2}$$

where $r_0(\theta)$ is the radial function and $r_0(\theta)$ has the following form of the Fourier expansion

$$r_0(\theta)=a_0+\sum_{j=1}^{J}(a_j\cos j\theta+b_j\sin j\theta). \tag{3.3}$$

In 3D, we assume that the scatterer D_0 is a revolving body with boundary Γ_0 through rotating the above 2D shape. Hence the corresponding parameterization in 2D can be straightforwardly applied to the case of 3D.

Definition 3.2. *The output of the neural network is defined as*

$$Y=\{Y_1,Y_2,\cdots,Y_{N_Y}\}\in\mathbb{R}^{N_Y}. \tag{3.4}$$

In 2D, for the reconstruction of the shape of the scatterer, $Y=\{a_0,a_1,b_1,\cdots,a_J,b_J\}$ and $N_Y=2J+1$. For the simultaneous reconstruction of the refractive index and shape, $Y=\{n_0,a_0,a_1,b_1,\cdots,a_J,b_J\}$ and $N_Y=2J+2$. In 3D, the parameters of model output are similar to 2D from the perspective of a revolving body.

In what follows, we present the main ingredients in the deep residual neural network which consists of many residual blocks. Compared to the plain network, the deep residual learning effectively avoids the degradation problem with the increasing

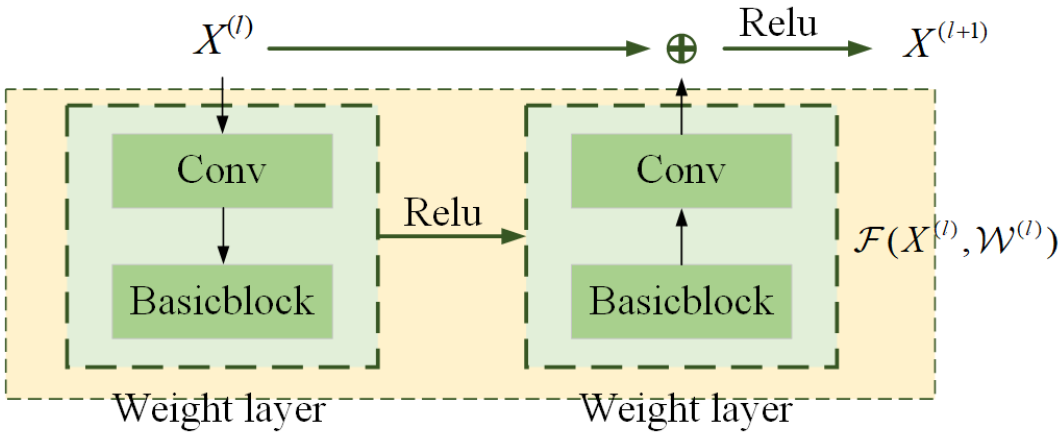

Figure 2: Structure of the residual block.

of network depth by the shortcut connections. See Fig. 2 for the structure of the residual block. The calculation formula is as follows

$$h^{(l)} = X^{(l)} + \mathcal{F}(X^{(l)}, \mathcal{W}^{(l)}), \tag{3.5a}$$

$$X^{(l+1)} = f(h^{(l)}), \tag{3.5b}$$

where $X^{(l)}$ and $X^{(l+1)}$ are the input and output of the lth residual unit, $\mathcal{W}^{(l)}$ is the weight set which depends on the number of layers in the lth residual unit. $\mathcal{F}$ denotes the residual function which consists of some convolutional layers. f denotes the rectified linear units activation function $f = \max(0,x)$. For the update of the weights, we define the loss function as

$$E(Y,\hat{Y}) = \frac{1}{P}\sum_{p=1}^{P} \|Y^{(p)} - \hat{Y}^{(p)}\|^2_{\mathbb{R}^{N_Y}}, \tag{3.6}$$

where P is the total number of samples, $Y^{(p)}$ and $\hat{Y}^{(p)}$ are the exact output and predicted output of the pth sample in the network, respectively. The norm $\|A\|_{\mathbb{R}^{N_Y}}$ satisfies $\|A\|_{\mathbb{R}^{N_Y}} = \sqrt{(A,A)}$ and (A,A) means the standard inner-product in $\mathbb{R}^{N_Y}$. A global average pooling layer (Avg-Pool) and a fully-connected layer (FC) are behind the above discussed residual blocks. See Fig. 3 for the illustration of the neural network model. It is clear that the main target of deep residual neural network is to minimize the loss function $E(Y,\hat{Y})$ to obtain the corresponding weights. We introduce the update of $\mathcal{W}^{(l)}$ as a example with gradient descent. Other weights are updated in the same way. Starting from a random initial weight $\mathcal{W}_0^{(l)}$, the sequence

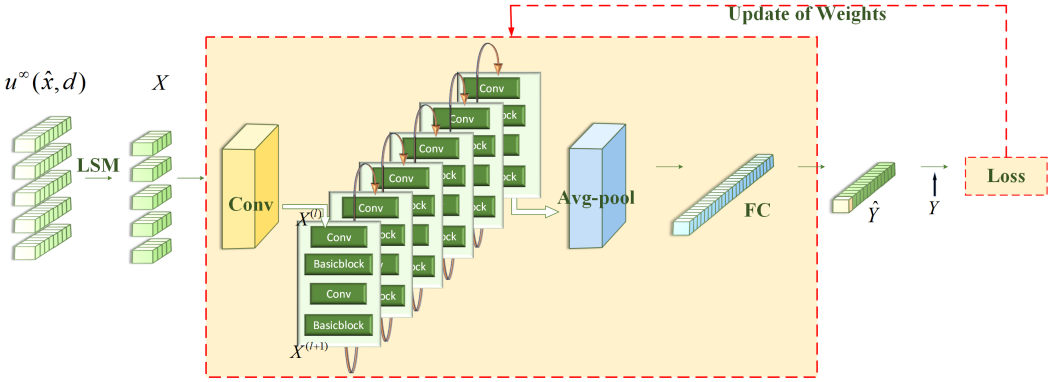

Figure 3: A schematic illustration of the neural network model.

of the weights $\{\mathcal{W}_m^{(l)}\}_{m=1}^M$ is calculated iteratively by

$$\mathcal{W}_{m+1}^{(l)} = \mathcal{W}_m^{(l)} + \Delta\mathcal{W}_m^{(l)}, \tag{3.7a}$$

$$\Delta\mathcal{W}_m^{(l)} = -\eta \frac{\partial E(Y,\hat{Y})}{\partial \mathcal{W}^{(l)}}, \tag{3.7b}$$

where

$$\frac{\partial E(Y,\hat{Y})}{\partial \mathcal{W}^{(l)}} = \frac{\partial E(Y,\hat{Y})}{\partial X^{(l+1)}} \frac{\partial X^{(l+1)}}{\partial h^{(l)}} \frac{\partial h^{(l)}}{\partial \mathcal{W}^{(l)}}, \quad m=0,1,\cdots,M,$$

and M represents the maximum number of epochs, η is the learning rate. If f is also an identity mapping: $X^{(l+1)}=h^{(l)}$, the form of the update of the weights can be changed appropriately. The details of our neural network are given as follows and dubbed as Algorithm 3.1.

Algorithm 3.1.

Step 1. Generate the network input X by LSM within certain wavenumber interval.

Step 2. Select a suitable parameterization form for 2D and 3D to generate the network output Y.

Step 3. Train the neural network from the generated input and output data.

Step 4. Determine the refractive index and shape information by the recovered transmission eigenvalues.

4 Numerical examples

In this section, some numerical experiments are presented to demonstrate the effectiveness of the proposed method. To solve Eq. (2.4), an adaptive regularisation method is used to adjust the regularisation parameter, which is used to control the smoothness of the solution. In 2D, the boundary integral equation method is employed to compute the far-field measurements $u^\infty(\hat{x}_{m_0},d_{n_0})$, $m_0=1,2,\cdots,M_0$, $n_0=1,2,\cdots,N_0$, where M_0 and N_0 respectively denote the number of incident direction and observation direction. We take $M_0=N_0=32$. In 3D, the corresponding settings are similar to the cases of 2D. The noisy data is given by

$$u^{\infty,\sigma}(\hat{x},d)=u^\infty(\hat{x},d)(1+\sigma\Delta), \tag{4.1}$$

where σ is the noise level and we take $\sigma=1\%$ in all the following examples. $\triangle$ is a random number generated by the normal distribution with mean 0 and standard deviation 1. The Fourier expansion term is chosen as $J=4$. The structures of the neural network are shown in Table 1. N_{FC} depends on the size of the model input and output. Three residual blocks are taken into account. $\rho\in[1,P]$ samples are randomly selected for batch training. The corresponding hyper parameters for the network are set and listed in Table 2. The model weights are updated by stochastic gradient descent algorithm.

Table 1: The structures of the network model.

Name	Conv	Residual Block-1	Residual Block-2	Residual Block-3	FC
Structure	$1\times3,8$	$\begin{bmatrix}1\times3,16\\1\times3,16\end{bmatrix}\times2$	$\begin{bmatrix}1\times3,32\\1\times3,32\end{bmatrix}\times2$	$\begin{bmatrix}1\times3,64\\1\times3,64\end{bmatrix}\times2$	$N_{FC}\times N_Y$

Table 2: Hyper parameters of the network.

Hyper parameter	P	ρ	η	M
Value	10000	100	10^{-3}	1000

4.1 Example 1

In this example, we consider three distinct shapes: peanut, pear, and flower, denoted as D_0^1, D_0^2 and D_0^3, respectively. The scatterers are located at the origin with boundary

$$\Gamma_0^1:=\left\{0.401\sqrt{4.331\cos^2t+\sin^2t}(\cos t,\sin t):\ t\in[0,2\pi]\right\},$$

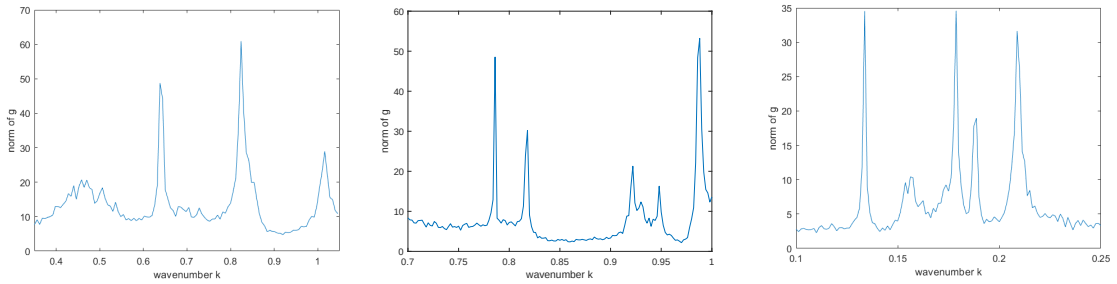

(a) (b) (c)

Figure 4: The plot of the norm of g for 2D scatters. (a) is the plot of the norm of g for the peanut with index $n_0^1=100.98$ at the fixed sampling point $(0.6,0.1)$. (b) is the plot of the norm of g for the pear-shaped scatterer with index $n_0^2=100$ at the fixed sampling point $(0.4,0.4)$. (c) is the plot of the norm of g for the flower-shaped scatterer with index $n_0^3=100.9$ at the fixed sampling point $(0.6,0.6)$.

$$\Gamma_0^2:=\{(1+0.15\sin 3t)(\cos t,\sin t):\ t\in[0,2\pi]\},$$
$$\Gamma_0^3:=\{(0.436+4.327\sin 4t)(\cos t,\sin t):\ t\in[0,2\pi]\}.$$

We set the interval I and wavenumbers are equally distributed within I for the determination of transmission eigenvalue. Using the linear sampling method at fixed sampling point, we obtain transmission eigenvalues. The specific settings are as follows in the Table 3.

The four determined transmission eigenvalues of the peanut, obtained through the linear sampling method at the fixed sampling point $(0.6,0.1)$, are $k_1=0.452$, $k_2=0.644$, $k_3=0.824$, and $k_4=1.016$. The determined five transmission eigenvalues of the pear are $k_1=0.786$, $k_2=0.816$, $k_3=0.922$, $k_4=0.948$ and $k_5=0.988$ at fixed sampling point $(0.4,0.4)$. The determined five transmission eigenvalues of the flower are $k_1=0.1337$, $k_2=0.1550$, $k_3=0.1787$, $k_4=0.1887$ and $k_5=0.2087$ by the linear sampling method at fixed sampling point $(0.6,0.6)$. The plot of the norm of g are shown in Fig. 4.

See Figs. 5(a), (d) and (g) for the exact physical configuration. Figs. 5(b), (e) and (h) show the reconstructions of boundary Γ_0^1, Γ_0^2 and Γ_0^3, respectively. Figs. 5(c), (f) and (i) show the simultaneous reconstructions of refractive index $\tilde{n}_0^1$, $\tilde{n}_0^2$, $\tilde{n}_0^3$ and

Table 3: Settings of 2D scatterers.

	n_0	I	wavenumber	sample point
peanut	100.98	[0.35,1.05]	117	(0.6,0.1)
pear	100	[0.7,1]	151	(0.4,0.4)
flower	100.9	[0.1,0.25]	121	(0.6,0.6)

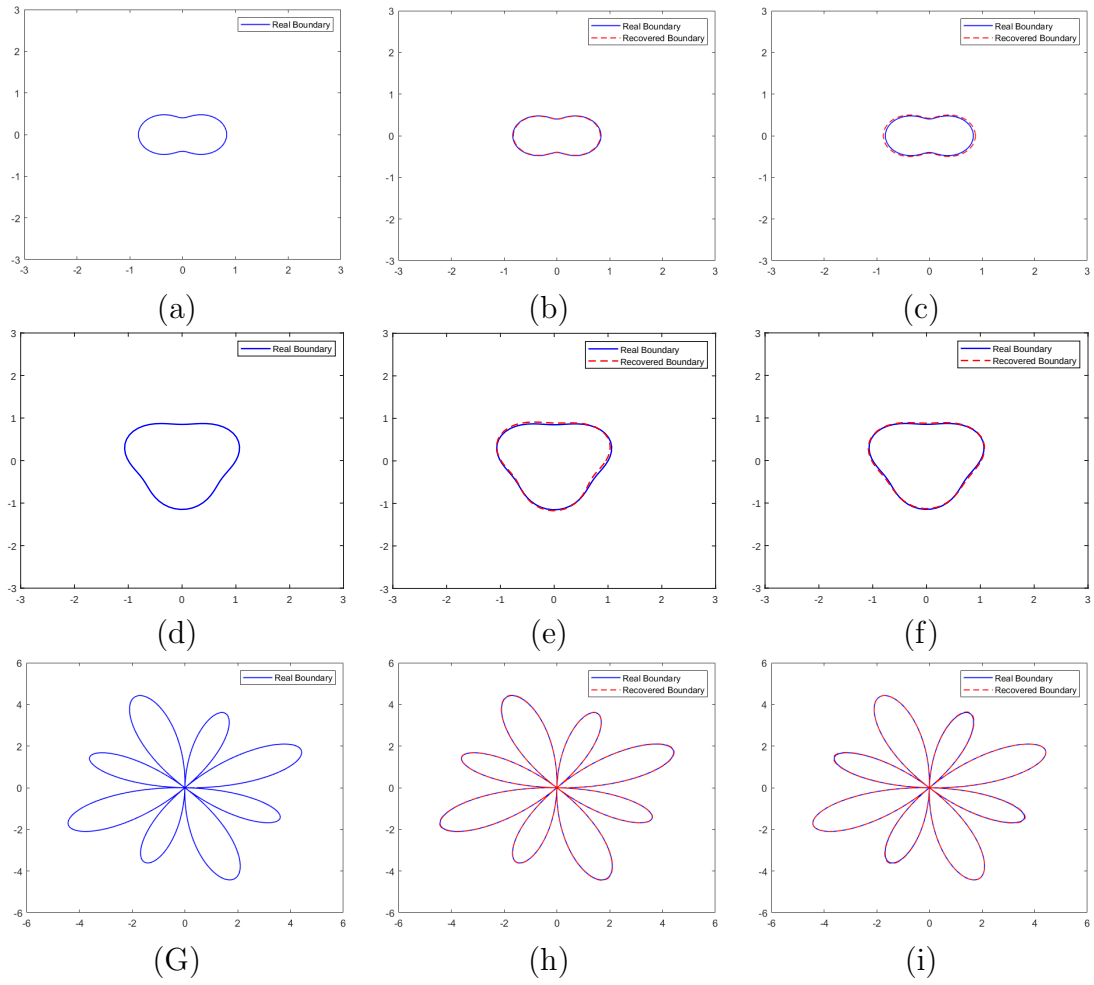

Figure 5: The reconstructions of 2D scatterers D_0^1, D_0^2 and D_0^3. (a) is the exact physical configuration of the peanut. (b) is the reconstruction for the boundary Γ_0^1. (c) is the simultaneous reconstructions for the refractive index $\tilde{n}_0^1$ and the boundary Γ_0^1. (d) is the exact physical configuration of the pear. (e) is the reconstruction for the boundary Γ_0^2. (f) is the simultaneous reconstructions for the refractive index $\tilde{n}_0^2$ and the boundary Γ_0^2. (g) is the exact physical configuration of the flower. (h) is the reconstruction for the boundary Γ_0^3. (i) is the simultaneous reconstructions for the refractive index $\tilde{n}_0^3$ and the boundary Γ_0^3.

boundary Γ_0^1, Γ_0^2, Γ_0^3, respectively.

The recovered results of refractive index are $\tilde{n}_0^1$=100.99, $\tilde{n}_0^2$=99.341, $\tilde{n}_0^3$=100.49. These results fully illustrate that our method can work well for the scatterer without a thin coating and can generate certain super-resolution effects because the size of scatterer is much smaller than the underlying wavelength, $2\pi/k$.

4.2 Example 2

In this example, we assume D_0^4, D_0^5 and D_0^6 are respectively 2D scatters with the thin coatings D_1^1, D_1^2 and D_1^3. The boundaries are given as follows

$$\begin{aligned}
&\Gamma_0^4 := \{(\cos t, \sin t) : \ t \in [0, 2\pi]\},\\
&\Gamma_1^1 := \{1.15(\cos t, \sin t) : \ t \in [0, 2\pi]\},\\
&\Gamma_0^5 := \{0.4\sqrt{4\cos^2 t + \sin^2 t}(\cos t, \sin t) : \ t \in [0, 2\pi]\},\\
&\Gamma_1^2 := \{(0.9\cos t, 0.7\sin t) : \ t \in [0, 2\pi]\},\\
&\Gamma_0^6 := \{(0.058 + 0.554\sin 4t)(\cos t, \sin t) : \ t \in [0, 2\pi]\},\\
&\Gamma_1^3 := \{(0.9\cos t, 0.7\sin t) : \ t \in [0, 2\pi]\}.
\end{aligned}$$

The specific settings are as follows in the Table 4. The determined five transmission eigenvalues of the peanut with the thin coating by the linear sampling method at fixed sampling point (0.3,0.2) are $k_1 = 0.754$, $k_2 = 0.781$, $k_3 = 0.799$, $k_4 = 0.847$ and $k_5 = 0.928$. The refractive index in D_0^4 and D_1^1 are $n_0^4 = 4$ and $n_1^1 = 280$. The four determined transmission eigenvalues of the pear with the thin coating, obtained through the linear sampling method at the fixed sampling point (0.1,0.1), are $k_1 = 0.530$, $k_2 = 0.710$, $k_3 = 0.785$ and $k_4 = 0.970$. The refractive index in D_0^5 and D_1^2 are $n_0^5 = 5.25$ and $n_1^2 = 200$, respectively. The determined five transmission eigenvalues of the flower with the thin coating at fixed sampling point (0.1,0.1) are $k_1 = 0.845$, $k_2 = 0.980$, $k_3 = 1.235$, $k_4 = 1.490$ and $k_5 = 1.505$. The refractive index in D_0^6 and D_1^3 are $n_0^6 = 6.17$ and $n_1^3 = 200$, respectively. The plot of the norm of g are shown in Fig. 6.

See Figs. 7(a), (d) and (g) for the exact physical configuration of the scatters with the thin coatings. Figs. 7(b), (e) and (h) show the reconstructions of boundary Γ_0^4, Γ_0^5 and Γ_0^6, respectively. Figs. 7(c), (f) and (i) show the simultaneous reconstructions of refractive index $\tilde{n}_0^4$, $\tilde{n}_0^5$, $\tilde{n}_0^6$ and boundary Γ_0^4, Γ_0^5, Γ_0^6, respectively.

The recovered results of refractive index are $\tilde{n}_0^4 = 3.9669$, $\tilde{n}_0^5 = 5.08$, $\tilde{n}_0^6 = 6.25$. Clearly, we find that for the case of the scatterer with a thin coating, our method also has good reconstructions.

Table 4: Settings of 2D scatterers with the thin coating.

	n_0	n_1	I	wavenumber	sample point
peanut with the thin coating	4.00	280	[0.7,1]	101	(0.3,0.2)
pear with the thin coating	5.25	200	[0.5,1.2]	121	(0.1,0.1)
flower with the thin coating	6.17	200	[0.8,1.6]	121	(0.1,0.1)

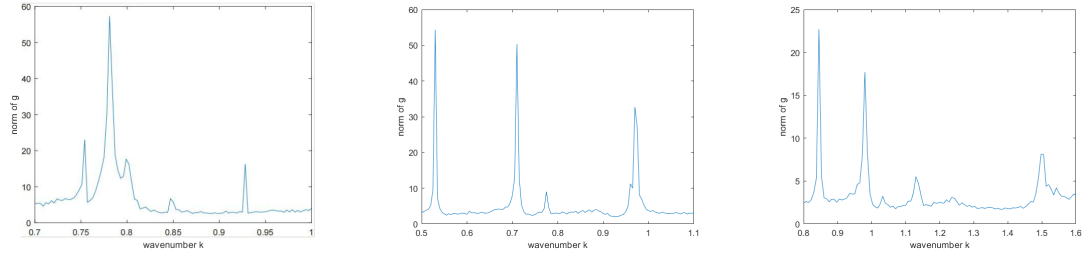

(a) (b) (c)

Figure 6: The plot of the norm of g for 2D scatters with thin coatings. (a) is the plot of the norm of g for peanut with index $n_0^4=4.00$ at the fixed sampling point $(0.3,0.2)$. (b) is the plot of the norm of g for pear-shaped scatterer with index $n_0^5=5.25$ at the fixed sampling point $(0.1,0.1)$. (c) is the plot of the norm of g for flower-shaped scatterer with index $n_0^6=6.17$ at the fixed sampling point $(0.1,0.1)$.

4.3 Example 3

In this example, D_0^7 is considered as a 3D peanut-shaped. The boundary D_0^7 is formed by rotating the two-dimensional peanut. Position the two-dimensional peanut on the xy-plane with its center at the origin, and rotate it in the direction of the positive x-axis. Due to the increased complexity of the three-dimensional problem compared to the two-dimensional one, we directly consider the 3D scatter with a high refractive index. Additionally, we consider to increase the number of transmission eigenvalues in the inverse problem. The refractive index in D_0^7 is n_0^7=100.04. The determined eight transmission eigenvalues are k_1=1.0277, k_2=1.0377, k_3=1.159, $k_4=1.2289$, $k_5=1.2313$, $k_6=1.3229$, $k_7=1.4562$ and $k_8=1.5348$. Fig. 8(a) shows the reconstructions of boundary Γ_0^7. Figs. 8(b)-(d) are the projections in the three directions of Fig. 8(a). Fig. 8(e) shows the simultaneous reconstructions of refractive index $\tilde{n}_0^7$ and boundary Γ_0^7. Figs. 8(f)-(h) are the projections in the three directions of Fig. 8(d). The recovered refractive index is $\tilde{n}_0^7=100.47$, demonstrating the effectiveness of our method in accurately capturing the refractive index variations from the original value $n_0^7=100.04$. These results fully illustrate that our method can work well for the general 3D scatterers.

4.4 Example 4

In this example, D_0^8 is considered as a 3D pear-shaped. The boundary D_0^8 is formed by rotating the two-dimensional pear. Position the two-dimensional pear on the xy-plane with its center at the origin, and rotate it in the direction of the positive x-axis. The refractive index in D_0^8 is n_0^8=100.95. The determined eight transmission

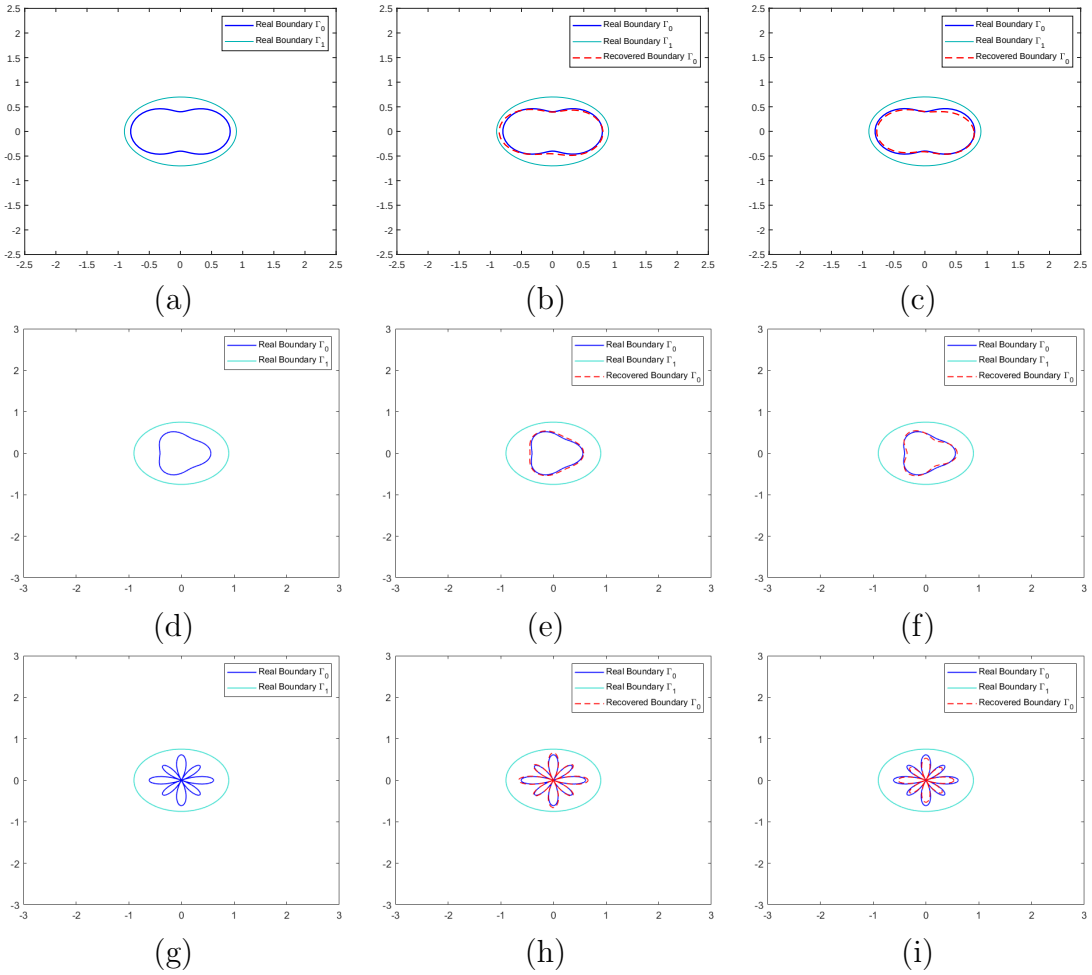

Figure 7: The reconstructions of 2D scatterers D_0^4, D_0^5 and D_0^6. (a) is the exact physical configuration of a peanut with the thin coating. (b) is the reconstruction for the boundary Γ_0^4. (c) is the simultaneous reconstructions for the refractive index $\tilde{n}_0^4$ and the boundary Γ_0^4. (d) is the exact physical configuration of a pear with the thin coating. (e) is the reconstruction for the boundary Γ_0^5. (f) is the simultaneous reconstructions for the refractive index $\tilde{n}_0^5$ and the boundary Γ_0^5. (g) is the exact physical configuration of a flower with the thin coating. (h) is the reconstruction for the boundary Γ_0^6. (i) is the simultaneous reconstructions for the refractive index $\tilde{n}_0^6$ and the boundary Γ_0^6.

eigenvalues are $k_1 = 1.2895$, $k_2 = 1.7854$, $k_3 = 1.8986$, $k_4 = 1.9832$, $k_5 = 2.4304$, $k_6 = 2.4951$, $k_7 = 2.7424$ and $k_8 = 2.870$. Fig. 9(a) shows the reconstructions of boundary Γ_0^8. Figs. 9(b)-(d) are the projections in the three directions of Fig. 9(a). Fig. 9(e) shows the simultaneous reconstructions of refractive index $\tilde{n}_0^8$ and boundary Γ_0^8. Figs. 9(f)-(h) are the projections in the three directions of Fig. 9(d). The recovered refractive index is $\tilde{n}_0^8 = 100.52$.

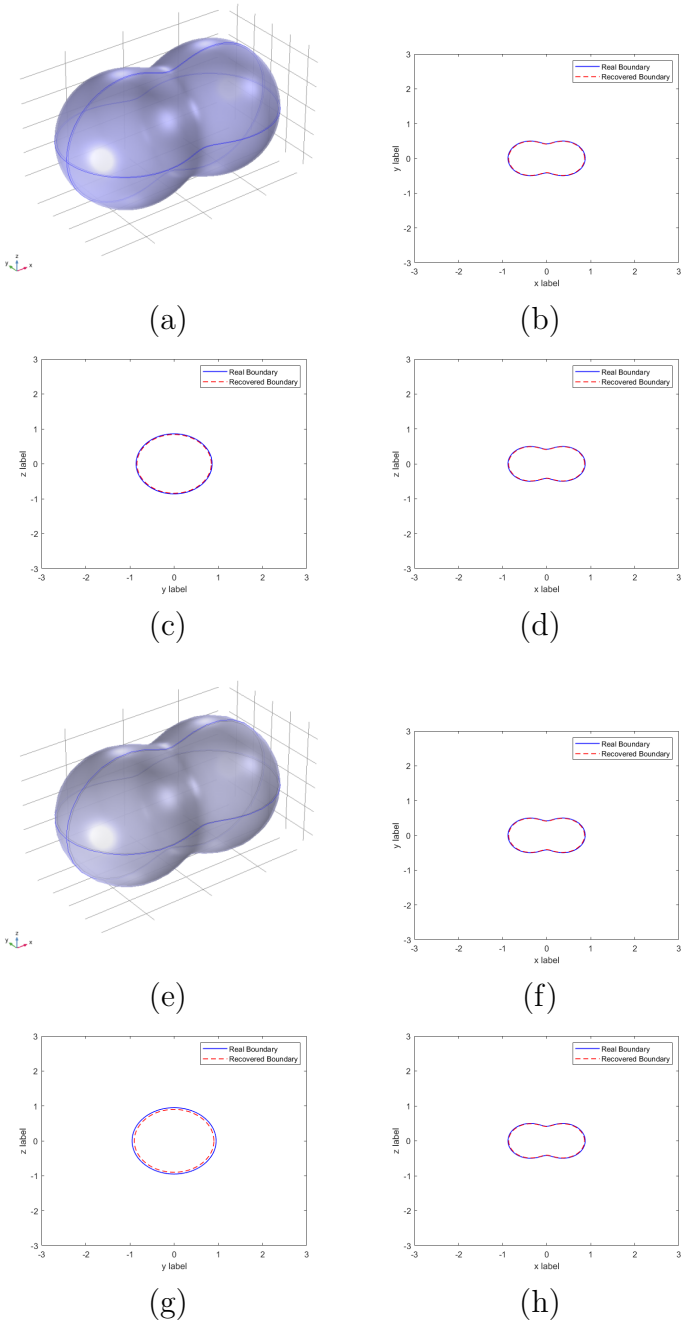

Figure 8: The reconstructions of the 3D peanut-shaped scatterer D_0^7. (a) is the reconstruction for the boundary Γ_0^7. (b)-(d) are projections in the three directions of (a). (e) is the simultaneous reconstructions for the refractive index $\tilde{n}_0^7$ and the boundary Γ_0^7. (f)-(h) are projections in the three directions of (b).

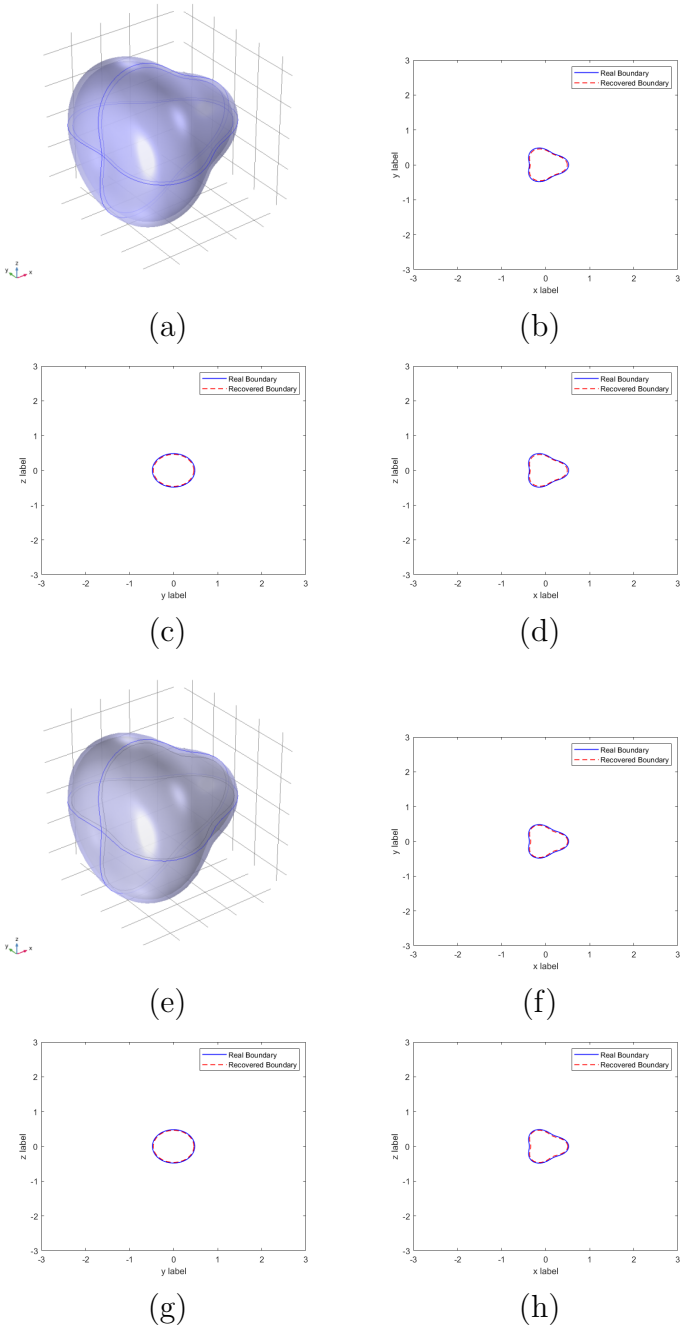

Figure 9: The reconstructions of the 3D pear-shaped scatterer D_0^8. (a) is the reconstruction for the boundary Γ_0^8. (b)-(d) are projections in the three directions of (a). (e) shows the simultaneous reconstructions of the refractive index $\tilde{n}_0^8$ and the boundary Γ_0^8. (f)-(h) are projections in the three directions of (b).

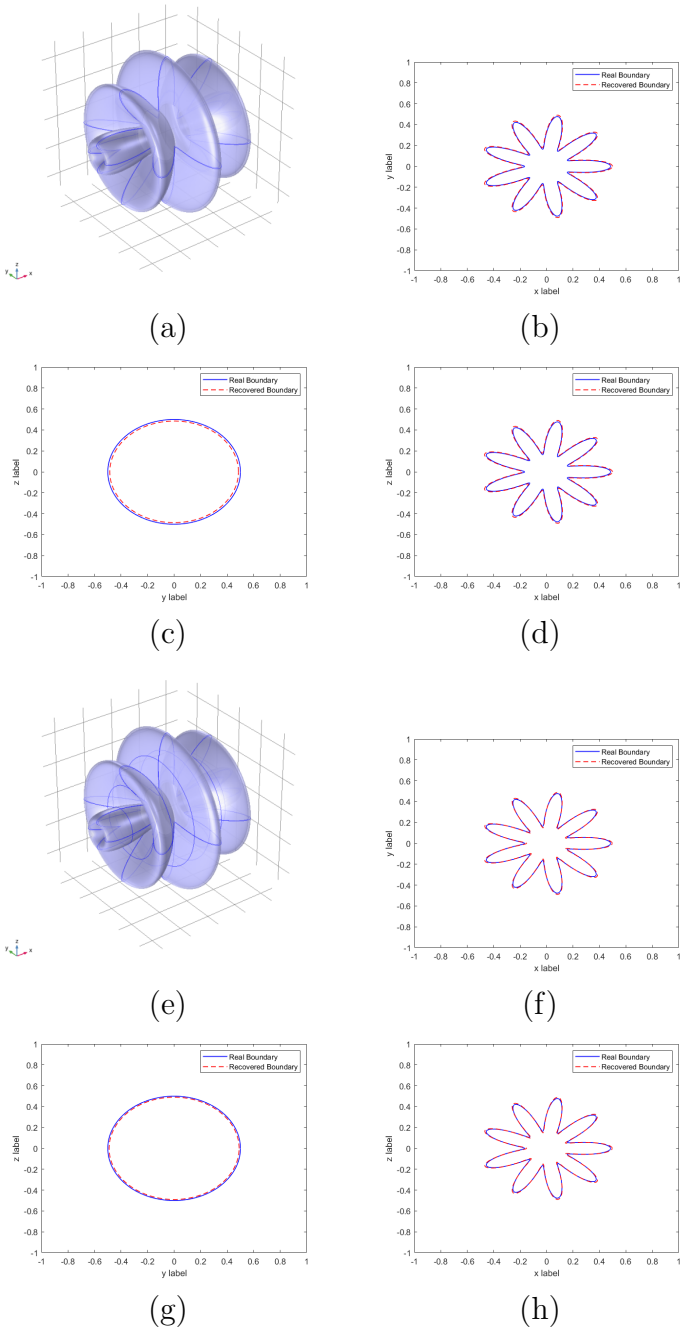

Figure 10: The reconstructions of the 3D flower-shaped scatterer D_0^9. (a) is the reconstruction for the boundary Γ_0^9. (b)-(d) are projections in the three directions of (a). (e) is the simultaneous reconstructions for the refractive index $\tilde{n}_0^9$ and the boundary Γ_0^9. (f)-(h) are projections in the three directions of (b).

4.5 Example 5

In this example, D_0^9 is considered as a 3D flower-shaped. The boundary D_0^9 is formed by rotating the two-dimensional flower. Position the two-dimensional flower on the xy-plane with its center at the origin, and rotate it in the direction of the positive x-axis. The refractive index in D_0^9 is n_0^9=100.85. The determined eight transmission eigenvalues are $k_1 = 5.0708$, $k_2 = 8.3243$, $k_3 = 8.3708$, $k_4 = 9.0326$, $k_5 = 11.989$, $k_6 = 12.579$, k_7=12.911 and k_8=13.037. Fig. 10(a) shows the reconstructions of boundary Γ_0^9. Figs. 10(b)-(d) are the projections in the three directions of Fig. 9(a). Fig. 10(e) shows the simultaneous reconstructions of refractive index $\tilde{n}_0^9$ and boundary Γ_0^9. Figs. 10(f)-(h) are the projections in the three directions of Fig. 10(d). The recovered refractive index is $\tilde{n}_0^9 = 100.36$.

5 Conclusions

In this paper, a two-step approach that combines LSM and neural networks is proposed for solving inverse interior transmission eigenvalue problems. The transmission eigenvalues are determined within a certain wavenumber interval by LSM. To avoid the different dimensions of the input in the neural network, we divide the wavenumber interval into several subintervals based on the transmission eigenvalues. Each transmission eigenvalue resides in the corresponding subinterval. The wavenumber, which yields the maximal value of the indicator function, constitutes the model input for our neural network. The refractive index and shape are regarded as the model output. Results from numerical experiments not only validate the effectiveness and promise of this two-step hybrid method but also reveal specific findings or effects. Furthermore, the small transmission eigenvalues in our method lead to a significant reduction in the size of the scatterer compared to the underlying wavelength, resulting in notable super-resolution effects. Hence, our method can generate certain super-resolution effects. However, our method requires a huge computational cost, especially for the case of 3D. In the future, we are committed to exploring a faster algorithm for determining the transmission eigenvalues. Other challenging and practical problems include extending our research to more difficult cases of elastic and electromagnetic transmission eigenvalue problems.

Acknowledgements

The work of Weishi Yin, Zhaobin Xu and Pinchao Meng was supported by the Jilin Natural Science Foundation, China (No. 20220101040JC) and the Na-

tional Natural Science Foundation of China (No. 12271207). The work of Hongyu Liu was supported by the Hong Kong RGC General Research Funds (projects 11311122, 12301420 and 11300821), the NSFC/RGC Joint Research Fund (project N_CityU 101/21), and the France-Hong Kong ANR/RGC Joint Research Grant, A_CityU203/19.

References

[1] H. Boujlida, H. Haddar and M. Khenissi, The asymptotic of transmission eigenvalues for a domain with a thin coating, SIAM J. Appl. Math., 78 (2018), 2348–2369.

[2] G. Bao and H. Liu, Nearly cloaking the electromagnetic fields, SIAM J. Appl. Math., 74 (2014), 724–742.

[3] G. Bao, H. Liu and J. Zou, Nearly cloaking the full Maxwell equations: cloaking active contents with general conducting layers, J. Math. Pures Appl., 101 (2014), 716–733.

[4] E. Blåsten, X. Li, H. Liu and Y. Wang, On vanishing and localizing of transmission eigenfunctions near singular points: a numerical study, Inverse Probl., 33 (2017), 105001.

[5] F. Cakoni, N. Chaulet and H. Haddar, Asymptotic analysis of the transmission eigenvalue problem for a Dirichlet obstacle coated by a thin layer of non-absorbing media, IMA J. Appl. Math., 80 (2015), 1063–1098.

[6] F. Cakoni and D. Colton, A Qualitative Approach to Inverse Scattering Theory, Springer-Verlag New York Heidelberg, 2014.

[7] F. Cakoni, D. Colton and H. Haddar, Inverse Scattering Theory and Transmission Eigenvalues, SIAM-Verlag Philadelphia Heidelberg, 2016.

[8] F. Cakoni, D. Colton and H. Haddar, On the determination of Dirichlet or transmission eigenvalues from far field data, C. R. Math., 348 (2010), 379–383.

[9] F. Cakoni and A. Kirsch On the interior transmission eigenvalue problem, Int. J. Comput. Sci. Math., 3 (2010), 142–167.

[10] Y. Chow, Y. Deng, Y. He, H. Liu and X. Wang, Surface-localized transmission eigenstates, super-resolution imaging, and pseudo surface plasmon modes, SIAM J. Imaging Sci., 14 (2021), 946–975.

[11] D. Colton and A. Kirsch, A simple method for solving inverse scattering problems in the resonance region, Inverse Probl., 12 (1996), 383–393.

[12] D. Colton and Y. Leung, On a transmission eigenvalue problem for a spherically stratified coated dielectric, Inverse Probl. Imaging, 10 (2016), 369–378.

[13] H. Diao, X. Cao and H. Liu, On the geometric structures of transmission eigenfunctions with a conductive boundary condition and applications, Commun. Partial Differential Equations., 46 (2021), 630–679.

[14] H. Diao, H. Li, H. Liu and J. Tang, Spectral properties of an acoustic-elastic transmission eigenvalue problem with applications, J. Differential Equations, 371 (2023),

629–659.
[15] Y. Gao and K. Zhang, Machine learning based data retrieval for inverse scattering problems with incomplete data, J. Inverse Ill-Posed Probl., 29 (2021), 249–266.
[16] Y. Gao, H. Liu, X. Wang and K. Zhang, On an artificial neural network for inverse scattering problems, J. Comput. Phys., 448 (2022), 110771.
[17] K. He, X. Zhang, S. Ren and J. Sun, Identity mappings in deep residual networks, in Proc. Eur. Conf. Comput. Vis., Springer International Publishing, Amsterdam, 2016.
[18] X. Ji and H. Liu, On isotropic cloaking and interior transmission eigenvalue problems, Euro. J. Appl. Math., 29 (2018), 253–280.
[19] A. Kirsch, The denseness of the far field patterns for the transmission problem, IMA J. Appl. Math., 37 (1986), 213–225.
[20] J. Li and H. Liu, Recovering a polyhedral obstacle by a few backscattering measurements, J. Differential Equations Appl., 259 (2015), 2101–2120.
[21] J. Li and H. Liu, Numerical Methods for Inverse Scattering Problems, Springer-Verlag Singapore Heidelberg, 2023.
[22] H. Liu, Schiffer's conjecture, interior transmission eigenvalues and invisibility cloaking: singular problem vs. nonsingular problem, Contemp. Math., 598 (2013), 147–154.
[23] H. Liu, On local and global structures of transmission eigenfunctions and beyond, J. Inverse Ill-posed Probl., 30 (2022), 287–305.
[24] H. Liu and C. Tsou, Stable determination by a single measurement, scattering bound and regularity of transmission eigenfunction, J. Inverse Ill-posed Probl., 61 (2022), 91.
[25] H. Liu, Y. Wang and S. Zhong, Nearly non-scattering electromagnetic wave set and its application, Z. Angew. Math. Phys., 68 (2017), 1–15.
[26] P. Meng, X. Wang and W. Yin, ODE-RU: A dynamical system view on recurrent neural networks, Electron Res. Arch., 30 (2022), 257–271.
[27] P. Meng, L. Wang, W. Yin and L. Zhou, A novel recurrent neural network of gated unit based on Euler's method and application, Commun. Anal. Comput., 1 (2023), 116–134.
[28] N. Pallikarakis and A. Ntargaras, Application of machine learning regression models to inverse eigenvalue problems, Comput. Math. Appl., 154 (2024), 162–174.
[29] J. Sun, Iterative methods for transmission eigenvalues, SIAM J. Numer. Anal., 49 (2011), 1860–1874.
[30] W. Yin, Z. Yang and P. Meng, Solving inverse scattering problem with a crack in inhomogeneous medium based on a convolutional neural network, Symmetry, 15 (2023), 119.
[31] Y. Yin, W. Yin, P. Meng and H. Liu, On a hybrid approach for recovering multiple obstacles, Commun. Comput. Phys., 31 (2022), 869–892.
[32] Y. Gao, H. Liu, X. Wang, and K. Zhang, A Bayesian scheme for reconstructing obstacles in acoustic waveguides, J. Sci. Comput., 97(3) (2023), 53.
[33] Y. Lin, H. Liu, and X. Liu, Determining a nonlinear hyperbolic system with unknown sources and nonlinearity. Journal of the London Mathematical Society, 109(2) (2024),

e12865.

[34] Y. Jiang, H. Liu, J. Zhang, and K. Zhang, Spectral patterns of elastic transmission eigenfunctions: boundary localization, surface resonance, and stress concentration, SIAM J. Appl. Math., 83(6) (2023), 2469–2498.

[35] R. Chen, Y. Deng, Y. Gao, J. Li, and H. Liu, Imaging multiple magnetized anomalies by geomagnetic monitoring, J. Comput. Phys., 498 (2024), 112661.

[36] H. Diao, R. Tang, H. Liu, and J. Tang, Unique determination by a single far-field measurement for an inverse elastic problem, (2023), arXiv preprint arXiv:2311.16435.